processes

MDPI

Article

Characterization of Refracturing Fracture Geometry and Production-Parameter Optimization Design for Low-Productivity Horizontal Shale Gas Wells in the H Block of Fuling

Peng Li [1,2], Yujia Liu [3], Yuqing Ma [3], Yiwen Guo [3], Chi Xu [1], Jiacheng Dai [1,3] and Shouceng Tian [1,3,*]

[1] National Key Laboratory of Petroleum Resources Engineering, China University of Petroleum (Beijing), Beijing 102249, China; li_p.jhyt@sinopec.com (P.L.); 18171431853@163.com (C.X.); daijc@cupk.edu.cn (J.D.)
[2] Sinopec Chongqing Fuling Shale Gas Exploration and Development Co., Ltd., Fuling District, Chongqing 408000, China
[3] Xinjiang Key Laboratory of Carbon Efficient Utilization and Storage, China University of Petroleum at Karamay, Beijing 834000, China; 15238991367@163.com (Y.L.); mayuqing0328@163.com (Y.M.); gywsydxhd@163.com (Y.G.)
* Correspondence: tscsydx@163.com

Abstract

Refracturing is an important stimulation technique for improving the productivity of mature shale gas wells. However, for low-productivity horizontal wells, the controlling effects of production history and pre-refracturing energy replenishment on fracture re-initiation and repropagation remain insufficiently quantified. This study focuses on mature wells in the H Block of the Fuling shale gas field. The Jiaoshiba area in the Fuling shale gas field, located on the eastern margin of the Sichuan Basin, is characterized by organic-rich marine shales of the Wufeng–Longmaxi Formation, where gas enrichment is jointly controlled by the Jiaoshiba anticline, fault distribution, and favorable preservation conditions. A three-dimensional geological model was constructed using seismic interpretation, well logging, core analysis, ant-tracking fracture attributes, and field fracturing data. A one-way coupled finite-element workflow was then applied to simulate the evolution of pore pressure and in situ stress during primary production, water-injection energy replenishment, and refracturing. The model was calibrated against historical bottomhole flowing pressure data, with a pressure-response matching accuracy greater than 85%. The results show that a lower initial production (4×10^4 m^3/d) allocation can mitigate reservoir pressure depletion and maintain a more favorable stress environment for fracture branching during refracturing. Compared with refracturing after 10 or 20 years of production, refracturing after 5 years produced a stronger post-treatment response in the simulated cases. For water-injection energy replenishment, an injection rate of 700 m^3/d restored reservoir pressure and regulated the local stress field more effectively than 500 m^3/d, whereas increasing the rate to 1000 m^3/d provided only limited additional pressure recovery. Overall, under the simulated reservoir conditions, a technically favorable parameter combination for the target well is an initial production allocation of 4×10^4 m^3/d, refracturing after approximately 5 years of production, and one year of pre-refracturing water-injection energy replenishment at about 700 m^3/d. These findings provide a reference for refracturing timing and pre-treatment energy-replenishment design in depleted shale gas reservoirs.

Keywords: shale gas; refracturing; fracture propagation; horizontal wells; shale gas of Fuling

Check for updates

Academic Editor: Chuanjin Yao

Received: 8 May 2026
Revised: 24 June 2026
Accepted: 26 June 2026
Published: 3 July 2026

Copyright: © 2026 by the authors. Licensee MDPI, Basel, Switzerland. This article is an open access article distributed under the terms and conditions of the Creative Commons Attribution (CC BY) license.

1. Introduction

China has abundant shale gas resources, with cumulative proved geological reserves reaching 2.95 trillion m^3 to date, and the development focus is accelerating toward deep shale formations and key blocks in southern China [1–3]. According to publicly available information released by Sinopec, by 2025, the Fuling shale gas field, a national-level demonstration project, had reported proven reserves of up to 1 trillion m^3 and had achieved large-scale commercial gas production and integrated technological deployment.

Among them, the Longmaxi Formation is characterized by ultra-low permeability, with an average permeability of approximately 14.5 μD [4–6], and therefore requires large-scale hydraulic fracturing to achieve economically viable production [7]. However, prolonged production results in gradual reservoir pressure depletion and a decline in fracture conductivity, ultimately leading to a substantial drop in production. For example, in a certain block of the Fuling shale gas field, the daily gas output declined from 20×10^4 m^3/d during the initial well-test period to 6×10^4 m^3/d after one year of production [8–10].

Refracturing, as an effective stimulation technology, has been widely applied to restore the productivity of low-producing wells and to increase the stimulated reservoir volume [11,12]. Previous studies have shown that refracturing is an important and effective restimulation measure for improving the production performance and ultimate recovery of unconventional oil and gas wells [13–15]. Among these factors, the initial production rate, initial production duration, and water injection rate for energy replenishment play key roles in controlling reservoir pressure, in situ stress redistribution, and fracture propagation [16–18].

Existing studies have demonstrated that the initial production rate plays a significant role in controlling refracturing fracture propagation behavior and final fracture geometry through its effect on reservoir pressure depletion and stress-field evolution [19,20]. With increasing initial production rate, the depleted zone becomes more pronounced and stress perturbation is intensified, thereby causing more substantial changes in refracturing fracture propagation direction and geometric characteristics [21–23]. Lake et al. (2014) used numerical simulations and field data analysis to study the impact of production rate on reservoir pressure [24]. They found that when the production rate increased from 200 stb/d to 500 stb/d, the pressure dropped from 3000 psi to 1700 psi within one year. At a lower production rate of 200 stb/d, the pressure decreased only to 2400 psi during the same period.

Initial production time influences the evolution of the in situ stress field, which in turn causes subsequent refracturing fractures to deviate and extend in altered directions during propagation [22,25]. Deng et al. (2024) used finite element simulations to study stress field reorientation in multi-fracture horizontal wells [26]. They found that as production time increased from 1 month to 4 years, the stress reorientation area expanded and then gradually shrank. This leads to fractures deviating and extending toward pressure-depleted areas during refracturing [27,28].

Meanwhile, numerous studies have shown that the water injection rate governs fracture propagation direction, balanced fracture growth, and fracture network geometry by affecting the degree of pressure restoration and stress-field reconstruction before and after refracturing, and therefore should be regarded as a key parameter in refracturing optimization [29]. Ren et al. (2022) used numerical simulation to study water injection for energy replenishment [30]. They found that the minimum horizontal principal stress increased by 1.2 MPa and 3.1 MPa at injection–production ratios of 0.2 and 1.2, respectively. This indicates that water injection can alter the stress field and affect fracture length after refracturing.

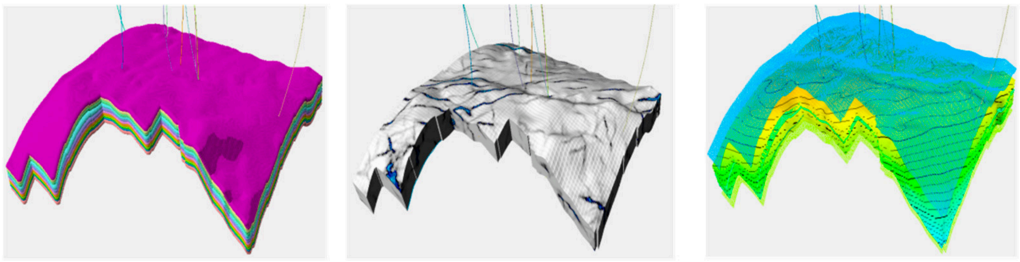
Existing studies on the Fuling shale gas block have demonstrated that refracturing performance is significantly governed by production-induced stress redistribution associated with reservoir pressure depletion. In 2024, Wang and colleagues developed a fully coupled seepage–geomechanical model using EDFM and the finite volume method. They optimized the refracturing timing based on shale gas well data from the Fuling field. The results showed that the proportion of the maximum horizontal principal stress reversal zone first increased and then decreased with time. They suggested that the optimal refracturing time for this well should be after 2000 days [31]. Appropriate initial production time and interval selection are conducive to improving fracture repropagation and production recovery [32], whereas different refracturing techniques, although capable of enhancing gas production, exhibit marked differences in stimulation effectiveness and engineering cost [33]. Despite these advances, few studies in the Jiaoshiba area of Fuling have quantitatively investigated how the initial production rate, initial production time, and water injection rate for energy replenishment affect stress redistribution prior to refracturing and the resulting post-refracturing fracture geometry. Therefore, this study proposes a one-way coupled finite element framework integrated with a discrete fracture network and a hydraulic fracture model. Using low-productivity horizontal wells in the H Block of the Fuling shale gas field as a case study, we evaluated how production parameters influence reservoir pressure, stress distribution, fracture propagation, and production performance prediction. The results provide both technical guidance and theoretical support for optimizing stimulation strategies in shale gas reservoirs of the H Block, Fuling.

2. Materials and Methods

2.1. Geological Model

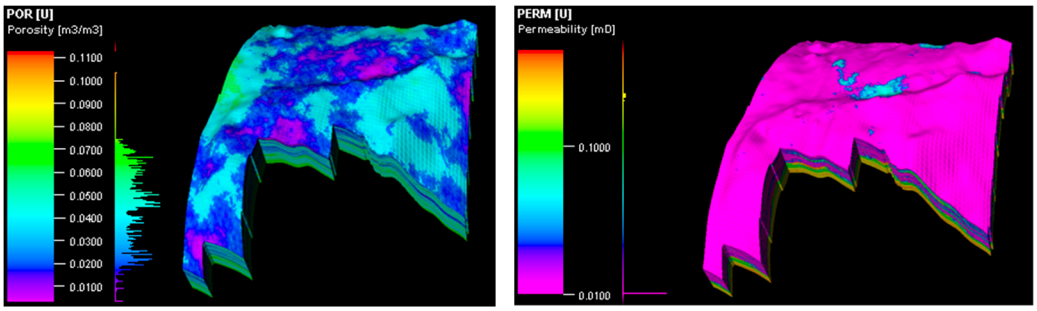
The study area is located in the H Block of the Fuling shale gas field in the Jiaoshiba area of the Sichuan Basin, southwestern China. The target Longmaxi shale interval occurs in a marine shale depositional system, and the burial depth of the modeled interval varies from approximately 1573 m to 2127 m. To characterize reservoir heterogeneity and structural geometry, a three-dimensional geological model was established for the Longmaxi shale formation was established using Petrel [2022] (SLB, Houston, TX, USA). The structural framework was constrained by seismic interpretation, well-to-seismic calibration, and ant-tracking attributes. The formation was vertically subdivided into 10 layers to preserve the main stratigraphic variations. A structural model was established in the depth domain, as shown in Figure 1a, and ant-tracking data were imported to describe the spatial distribution of natural fractures, as shown in Figure 1b. Considering interwell interference in the planar direction, the model employed a grid resolution of 10 m $\times$ 10 m to meet the requirements of fracture propagation and fluid-flow simulation. The final high-resolution geological model contains approximately 16 million grid cells, as shown in Figure 1c, and reproduces stratigraphic undulation, fault geometry, and variations in reservoir thickness. Based on seismic interpretation, fault interpretation, ant-tracking attributes, and well-log data, the spatial distribution characteristics and dominant orientations of natural fractures were identified. Faults and ant-tracking results were used to characterize the spatial heterogeneity of the natural fracture system. On this basis, a discrete fracture network (DFN) model was generated using key fracture parameters, including fracture orientation, dip angle, and length.

As shown in Figure 2, a three-dimensional reservoir property model was established based on well-log data and core analysis results, with porosity ranging from 0.003 to 0.113 and permeability from 0.01 to 0.45 mD, reflecting the typical low-porosity and low-permeability characteristics of the shale gas reservoir.



(**a**) (**b**) (**c**)

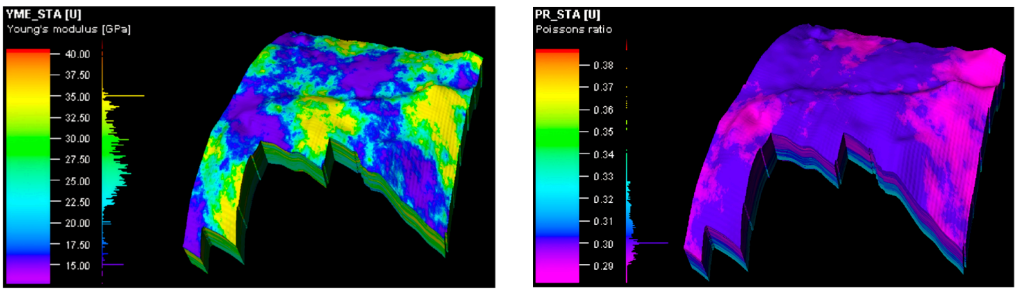
Figure 1. (**a**) Structural model in the depth domain; (**b**) imported ant-tracking data; (**c**) grid discretization.



(**a**) (**b**)

Figure 2. (**a**) Porosity; (**b**) permeability model.

To obtain the in situ stress field required for fracture propagation simulation, the Young's modulus (12–40 GPa) and Poisson's ratio (0.27–0.34) inverted from well-log data were incorporated into the geological model. These data were further integrated with well-bore stability analysis, microseismic event localization, and hydraulic fracturing treatment data to invert the three-dimensional in situ stress field, as shown in Figure 3.



(**a**) (**b**)

Figure 3. (**a**) Young's modulus; (**b**) Poisson's ratio model.

During the model construction process, the maximum horizontal principal stress, minimum horizontal principal stress, pore pressure, and overburden pressure were assigned ranges of 54–68 MPa, 45–57 MPa, 24–39 MPa, and 52–60 MPa, respectively, while their spatial variations were also taken into account. The initial minimum horizontal principal stress was oriented in the north–south direction. A stress calibration factor was applied to ensure consistency between the stress gradient and the regional tectonic stress, as shown in Figure 4. The resulting stress model shows that local stress variations exceeding 30 m exist within the main reservoir interval, providing essential input for evaluating refracturing-induced fracture deflection, effective fracture height control, and the effectiveness of reservoir stimulation.

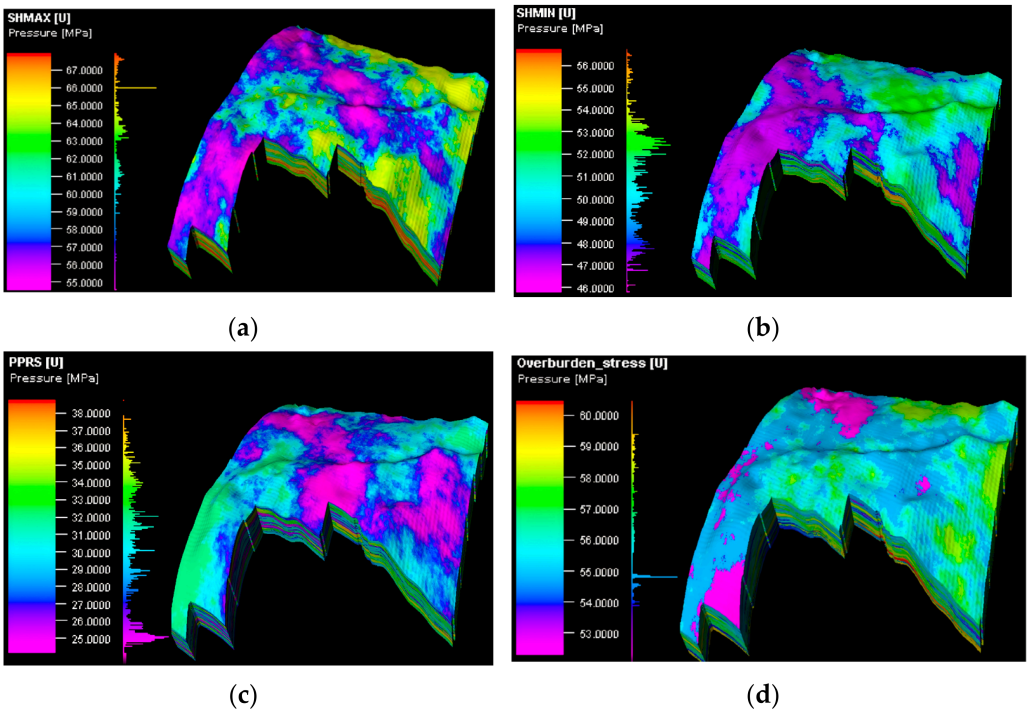


Figure 4. (**a**) Maximum horizontal principal stress; (**b**) minimum horizontal principal stress; (**c**) pore pressure; (**d**) overburden pressure model.

The specific reservoir and geomechanical parameters are listed in Table 1. It should be noted that the parameters in Table 1 are field-measured data adopted as equivalent parameters at the numerical model scale, which differ from the typical parameters used in the Introduction to describe engineering/geological-scale characteristics.

Table 1. Initial Reservoir Parameters.

Rock Mechanics Parameters		Gas Reservoir Model Parameters	
Overburden Pressure	52–60 MPa	Pore Pressure	24–39 MPa
Maximum Horizontal Principal Stress	54–68 MPa	Water Saturation	17–100%
Minimum Horizontal Principal Stress	45–57 MPa	Permeability	0.01–0.45 mD
Young's Modulus	12–40 GPa	Porosity	0.003–0.113
Poisson's Ratio	0.27–0.34		

2.2. Mathematical Model

During shale gas reservoir development, continuous changes in pore pressure induce effective stress redistribution, which further drives the dynamic evolution of the in situ stress field and flow field. Therefore, it is necessary to establish a mathematical model capable of simultaneously describing the coupling relationship between the flow field and the stress field, and to solve it using numerical methods.

Within the framework of poroelastic theory, this study establishes a mathematical model incorporating rock elastic-parameter inversion, pore-pressure evolution, in situ stress calculation, and flow-stress coupling. A one-way coupled finite-element workflow was used: reservoir-flow simulation first updated pore-pressure depletion or pressure recovery under production and injection schedules; the updated pore-pressure field was then transferred to the geomechanical model to calculate effective-stress redistribution; finally, the updated stress field was used as the initial condition for refracturing-fracture propagation simulation.

The outer boundaries of the reservoir model were treated as no-flow boundaries for the finite simulation domain, while the wellbore was represented by rate-controlled production or injection constraints according to the scenario design. The vertical overburden stress was imposed from density integration, and horizontal stress components were initialized from the calibrated geostress model. At each production or injection step, pressure changes were converted into effective-stress changes through the Biot poroelastic relationship. Numerical convergence was checked by monitoring pressure residuals, displacement/stress residuals, and material-balance consistency between successive coupled steps; simulations were advanced only after the coupled pressure-stress solution became stable for the specified time step.

The vertical in situ stress is mainly generated by the overburden weight of the overlying strata and can be obtained by integrating the formation density over depth [34]:

$$\sigma_v = \int_0^H \rho(h) g dh \tag{1}$$

This method can realistically capture the continuous variation in vertical stress with burial depth, thereby providing a fundamental constraint for the calculation of horizontal in situ stresses. where σ_v is the vertical stress (MPa); ρ(h) is the bulk density at depth h (kg/m^3); g is the gravitational acceleration (9.81 m/s^2); h is the burial depth (m); and H is the total burial depth used for integration (m). To describe the deformation behavior of shale reservoirs under production-induced stress conditions, this study assumes that the reservoir rock is a linear elastic orthotropic medium, and its stress–strain relationship can be expressed as follows [35]:

$$\varepsilon = S\sigma \tag{2}$$

where ε and σ denote the strain and stress tensors, respectively, and S is the compliance matrix, which can be expressed in the following form:

$$\begin{bmatrix} \varepsilon_{11} \\ \varepsilon_{22} \\ \varepsilon_{33} \\ \varepsilon_{23} \\ \varepsilon_{31} \\ \varepsilon_{12} \end{bmatrix} = \begin{bmatrix} \frac{1}{E_1} & -\frac{\nu_{21}}{E_2} & -\frac{\nu_{31}}{E_3} & 0 & 0 & 0 \\ -\frac{\nu_{12}}{E_1} & \frac{1}{E_2} & -\frac{\nu_{32}}{E_3} & 0 & 0 & 0 \\ -\frac{\nu_{13}}{E_1} & -\frac{\nu_{23}}{E_2} & \frac{1}{E_3} & 0 & 0 & 0 \\ 0 & 0 & 0 & \frac{1}{G_{23}} & 0 & 0 \\ 0 & 0 & 0 & 0 & \frac{1}{G_{31}} & 0 \\ 0 & 0 & 0 & 0 & 0 & \frac{1}{G_{12}} \end{bmatrix} \begin{bmatrix} \sigma_{11} \\ \sigma_{22} \\ \sigma_{33} \\ \sigma_{23} \\ \sigma_{31} \\ \sigma_{12} \end{bmatrix} \tag{3}$$

This constitutive relationship provides the mechanical basis for subsequent poroelastic stress calculation and the numerical solution of hydro-mechanical coupling.

Rock elastic parameters are key input variables in the poroelastic geo-stress model. In this study, Poisson's ratio and Young's modulus were inverted from compressional- and shear-wave transit-time data to ensure the spatial continuity and in situ applicability of the parameters.

(1) Poisson's Ratio Inversion

Poisson's ratio is calculated from the relationship between compressional- and shear-wave transit times:

$$\nu = \frac{1}{2}\left(\frac{\Delta t_s^2 - 2\Delta t_p^2}{\Delta t_s^2 - \Delta t_p^2}\right) \tag{4}$$

where ν is Poisson's ratio (dimensionless), Δt_p is the compressional-wave transit time (μs/m), and Δt_s is the shear-wave transit time (μs/m). This equation is based on elastic wave propagation theory and can effectively characterize the lateral deformability of the

rock, making Poisson's ratio an important parameter for evaluating reservoir brittleness and stress distribution characteristics [36].

(2) Young's Modulus Inversion

Based on Poisson's ratio, the rock Young's modulus is further inverted by incorporating formation density:

$$E_t = \left(\frac{\rho_b}{\Delta t_s^2}\right)\left(\frac{3\Delta t_s^2 - 4\Delta t_p^2}{\Delta t_s^2 - 2\Delta t_p^2}\right) \tag{5}$$

where ρ_b denotes the bulk density of the formation.

This model can reflect the vertical heterogeneity of the reservoir and serves as an important mechanical parameter controlling fracture width and conductivity [36].

After the fractured well is put into production, the pore pressure of the shale gas reservoir continuously declines with increasing production time, thereby causing changes in effective stress and the in situ stress field [37]. The evolution of pore pressure is described using an exponential decline model:

$$p_p = p_o - (p_o - p_b)\left(\frac{\Delta t_n}{\Delta t_0}\right)^N \tag{6}$$

where p_o denotes the initial pore pressure, p_b is the boundary pressure, Δt_n represents the current production time, and N is the pressure decline exponent.

This model can capture the characteristic pressure depletion behavior of unconventional reservoirs and provides a dynamic pressure boundary for stress recovery and fracture reactivation under refracturing conditions.

Based on the obtained vertical in situ stress, elastic parameters, and pore pressure, and within the framework of poroelastic theory [38], the minimum and maximum horizontal principal stresses can be expressed as follows:

$$\sigma_h = \frac{u_v E_h}{(1-u_h)E_v}(\sigma_v - \alpha p_p) + \alpha p_p + \frac{E_h \varepsilon_h}{1-u_h^2} + \frac{u_v E_h \varepsilon_H}{1-u_h^2} \tag{7}$$

$$\sigma_H = \frac{u_v E_h}{(1-u_h)E_v}(\sigma_v - \alpha p_p) + \alpha p_p + \frac{E_h \varepsilon_H}{1-u_h^2} + \frac{u_v E_h \varepsilon_h}{1-u_h^2} \tag{8}$$

where σ_h, σ_H denote the minimum and maximum horizontal principal stresses, respectively; E_h, E_v are the Young's moduli in the horizontal and vertical directions, respectively; u_h, u_v represent Poisson's ratios in the horizontal and vertical directions, respectively; α is the Biot effective stress coefficient; and ε_h and ε_H are the tectonic strain terms.

2.3. Numerical Simulation

In this study, field data were used as the basis for simulating formation properties, fracture development characteristics, and their effects on production performance. The numerical cases were divided into three groups: initial production-rate cases, primary production-time cases, and pre-refracturing water-injection cases. During the initial production stage, production simulations were conducted for Well JY5-1HF under different production parameters to analyze variations in in situ stress and reservoir pressure.

In the water-injection energy-replenishment cases, the production well was converted to an injection well, and different water-injection rates were assigned to simulate different energy-replenishment rates. After each production or injection scenario, the refracturing parameters of Well JY5-1HF, including perforation scheme and pumping schedule, were applied according to field treatment design data from the block. Therefore, the perforation and pumping schedules represent field-based treatment-design inputs rather than arbitrary

assumed values. The resulting refracturing simulations were used to investigate fracture evolution patterns and production response after refracturing.

Refracturing was conducted using a multi-stage, multi-cluster stimulation scheme, and the perforation parameters were specified in accordance with the field treatment design of the block. Two perforation clusters were arranged in each fracturing stage, with 12 perforation shots in each cluster. The perforation diameter was uniformly set to 10.67 mm, the perforation tunnel length was 203.20 mm, and the perforation phasing angle was set at 60°. The perforation clusters were uniformly distributed along the horizontal section to ensure similar fracture initiation conditions for each fracture within a stage, thereby minimizing the influence of nonphysical factors on the simulation results. The detailed perforation parameters are listed in Table 2.

Table 2. Perforation Parameters.

Perf Top MD (m)	Perf Bottom MD (m)	No of Shots	Perf Diam (mm)
2893.06	2893.67	12	10.67
2932.72	2933.33	12	10.67
2972.39	2973.00	12	10.67
3012.06	3012.67	12	10.67
3051.72	3052.33	12	10.67
3091.39	3092.00	12	10.67
3131.06	3131.67	12	10.67
3170.72	3171.33	12	10.67

For the pumping schedule, this study selected HCl as the pad fluid, with a total pad volume of 1 m^3. The slurry stage consisted of a mixture of HCl and slickwater, and quartz sand was used as the proppant throughout the treatment. First, 9 m^3 of HCl was injected at a proppant concentration of 7 kg/PA using 30/50 mesh quartz sand, followed by 1654.41 m^3 of slickwater at a proppant concentration of 40.45 kg/PA with 40/70 mesh quartz sand. The displacement stage consisted of 200 m^3 of brine, with a proppant concentration of 3.06 kg/PA and 30/50 mesh quartz sand. The pumping rate was uniformly set at 12.10 m^3/min throughout the treatment.

2.4. History Matching

Using the artificial intelligence-based history-matching capability and GPU-accelerated high-performance computing of Zfrac, the geomechanical model was calibrated against historical bottomhole flowing pressure data for Well JY5-1HF during the initial production period from 1 January 2013 to 1 October 2025, as shown in Figure 5. The historical production schedule was used as the operating constraint, while bottomhole flowing pressure was used as the main matching target. The reported matching accuracy greater than 85% was calculated from the normalized deviation between simulated and measured bottomhole flowing pressure, indicating that the model can reproduce the main pressure-depletion trend during long-term production. When the simulated curve can reasonably reproduce the overall trend, decline characteristics, and major inflection points of the actual production curve, and when the overall deviation of key indicators remains within 15%, the model is considered to achieve approximately 85% history-matching accuracy. This criterion is used to characterize the model's ability to reproduce actual production behavior, rather than to evaluate the absolute error at a single time point.

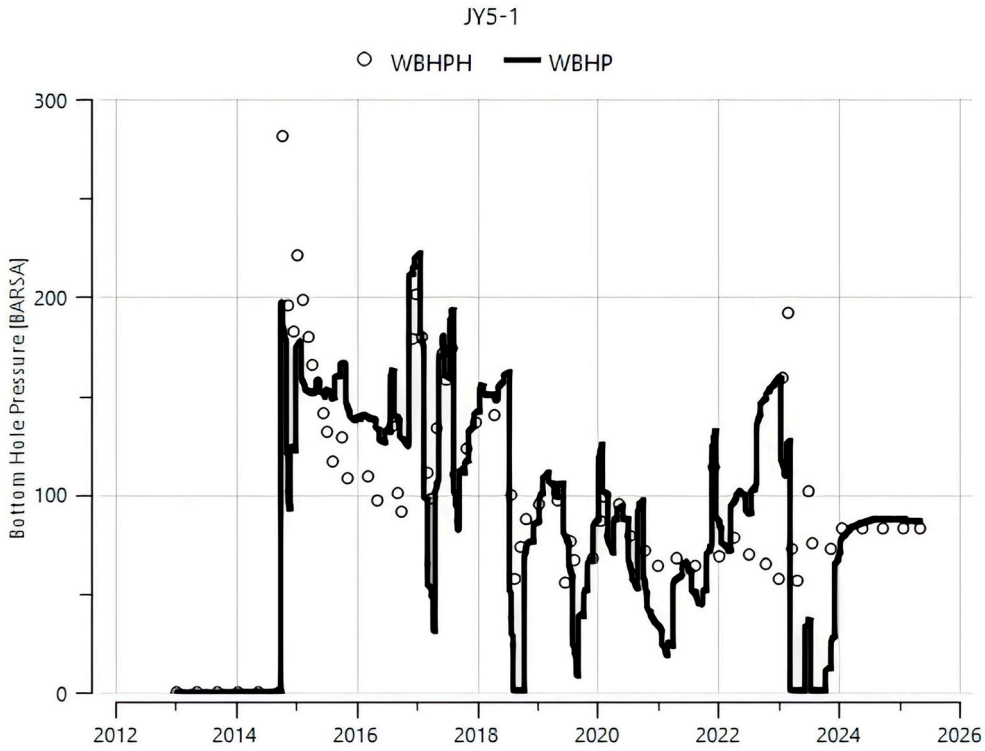


Figure 5. History-matching curve of bottomhole flowing pressure data for Well JY5-1.

3. Results and Discussion

3.1. Simulation Results and Interpretation: Initial Production Rate

This subsection evaluates how the imposed initial production rate changes reservoir-pressure depletion, stress redistribution, refracturing fracture geometry, and post-refracturing production response. The production period was fixed at 5 years, and the initial production rate was varied among 4×10^4, 20×10^4, and 30×10^4 m^3/d so that the effect of production rate could be isolated.

3.1.1. Effect of Initial Production Rate on Reservoir Pressure

After 5 years of production, the reservoir pressures at a distance of 4 m from the wellbore decreased to 22.02 MPa, 13.99 MPa, and 4.33 MPa, respectively. As shown in Figure 6, with increasing initial production rate, the pressure-depletion zone around the wellbore expands significantly, and the reservoir pressure continues to decline. The results indicate that a higher initial production rate intensifies reservoir-pressure depletion and leads to a greater pressure decline.

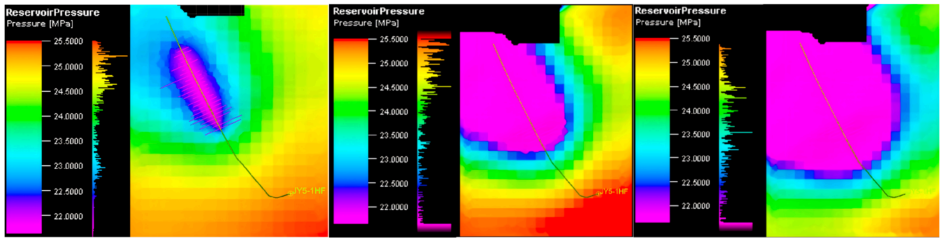
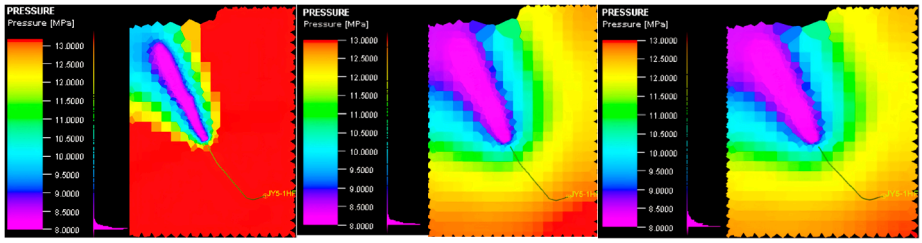


Figure 6. Reservoir pressure after 5 years of production following initial fracturing at initial production rates of (**a**) 4×10^4 m^3/d, (**b**) 20×10^4 m^3/d, and (**c**) 30×10^4 m^3/d.

After refracturing, the effects of different initial production rates on reservoir pressure depletion exhibit a generally consistent trend, although the magnitude of the effect remains controlled, as shown in Figure 7. Under initial production rates of 4×10^4 m^3/d, 20×10^4 m^3/d, and 30×10^4 m^3/d, the resulting reservoir pressures at a distance of 4 m from the wellbore after refracturing were 8.20 MPa, 8.07 MPa, and 8.14 MPa, respectively. The simulation results show that the degree of reservoir pressure depletion after refracturing is significantly weaker than that observed after long-term production following the initial fracturing treatment. This study suggests that refracturing reconnects previously unstimulated reservoir zones, thereby replenishing formation energy.

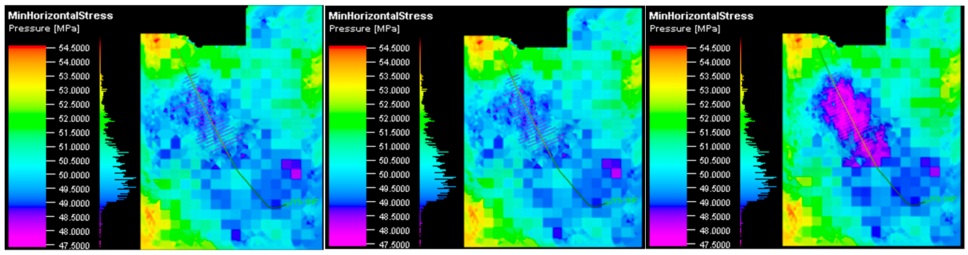


(**a**) (**b**) (**c**)

Figure 7. Reservoir pressure after 5 years of post-refracturing production at initial production rates of (**a**) 4×10^4 m^3/d, (**b**) 20×10^4 m^3/d, and (**c**) 30×10^4 m^3/d.

3.1.2. Effect of Initial Production Rate on In Situ Stress

After 5 years of production, the minimum horizontal principal stresses at a distance of 4 m from the wellbore decreased to 49.47 MPa, 48.95 MPa, and 47.60 MPa, respectively. As shown in Figure 8, with increasing initial production rate, the minimum horizontal principal stress near the fractures continuously decreases, and the stress-reoriented zone expands over a broader area under high-production conditions. These results indicate that a higher initial production rate promotes stronger in situ stress release and more extensive stress redistribution.



(**a**) (**b**) (**c**)

Figure 8. Distribution of minimum horizontal principal stress after 5 years of production following initial fracturing at production rates of (**a**) 4×10^4 m^3/d, (**b**) 20×10^4 m^3/d, and (**c**) 30×10^4 m^3/d.

After refracturing, the minimum horizontal principal stresses at a distance of 4 m from the wellbore decreased to 45.48 MPa, 45.25 MPa, and 45.06 MPa, respectively. As shown in Figure 9, refracturing expands the stress-depleted zone, and the stress-reoriented region exhibits an elliptical distribution, with more concentrated stress depletion under high-production conditions. The results indicate that refracturing can enlarge the stress-depleted area, whereas the magnitude of stress reduction tends to converge under high-production conditions.

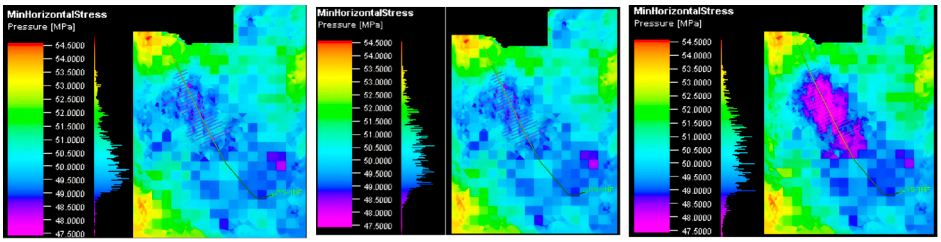


Figure 9. Distribution of minimum horizontal principal stress after 5 years of post-refracturing production at production rates of (**a**) 4×10^4 m^3/d, (**b**) 20×10^4 m^3/d, and (**c**) 30×10^4 m^3/d.

3.1.3. Effect of Initial Production Rate on Refracturing Fracture Geometry

Under the condition of refracturing after 5 years of production at a production rate of 4×10^4 m^3/d, the resulting fracture geometry is shown in Figure 10a. Fracture branching was observed, indicating that the initial fracture network had not been fully activated during the first stimulation. The secondary fracturing treatment was therefore able to reactivate the pre-existing fracture system and enhance the complexity of the fracture network. When the gas production rate was increased to 20×10^4 m^3/d, the resulting fracture geometry is shown in Figure 10b. It can be observed that the fracture network created during the initial fracturing treatment had been fully utilized, and a pressure-depletion funnel developed in the near-wellbore region. As a result, the refracturing fluid was readily drawn into the low-pressure zone, limiting fracture extension and leading to the formation of short fractures. When the production rate was further increased to 30×10^4 m^3/d, fracture propagation became significantly more restricted, and a greater number of short fractures were generated, as shown in Figure 10c. This study attributes this behavior to the depletion of formation energy caused by refracturing ultra-high-production wells.

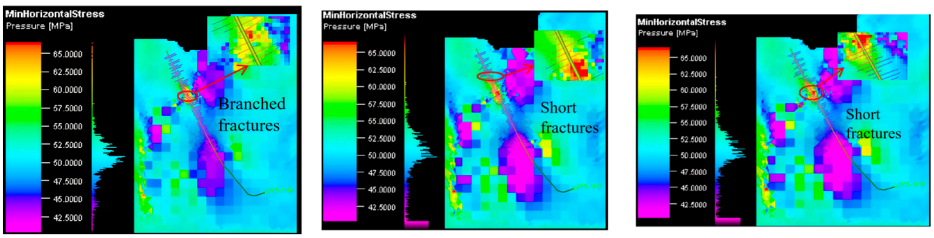


Figure 10. Fracture geometry and stress field overlay after 5 years of initial production at production rates of (**a**) 4×10^4 m^3/d, (**b**) 20×10^4 m^3/d, and (**c**) 30×10^4 m^3/d.

The distribution of average fracture length obtained after refracturing following 5 years of production at initial production rates of 4×10^4 m^3/d, 20×10^4 m^3/d, and 30×10^4 m^3/d is shown in Figure 11. The standard deviations of the average fracture length were 19.033, 34.334, and 39.565, respectively. The average fracture lengths were 98.476 m, 78.835 m, and 71.601 m, respectively. The results indicate that increasing production rate suppresses fracture propagation and leads to a more dispersed distribution of fracture lengths. This behavior can be attributed to the increase in initial production rate, which accelerates reservoir pressure depletion and ultimately intensifies reservoir pressure exhaustion. Values at a location 4 m from the wellbore were selected to provide a consistent comparison of the local near-wellbore responses among the different cases. Although the pressure and stress values at this location are relatively similar, marked differences exist in the spatial distributions of the pressure and stress fields and in the extent of stress reorientation, resulting in substantial variations in fracture length, height, and width.

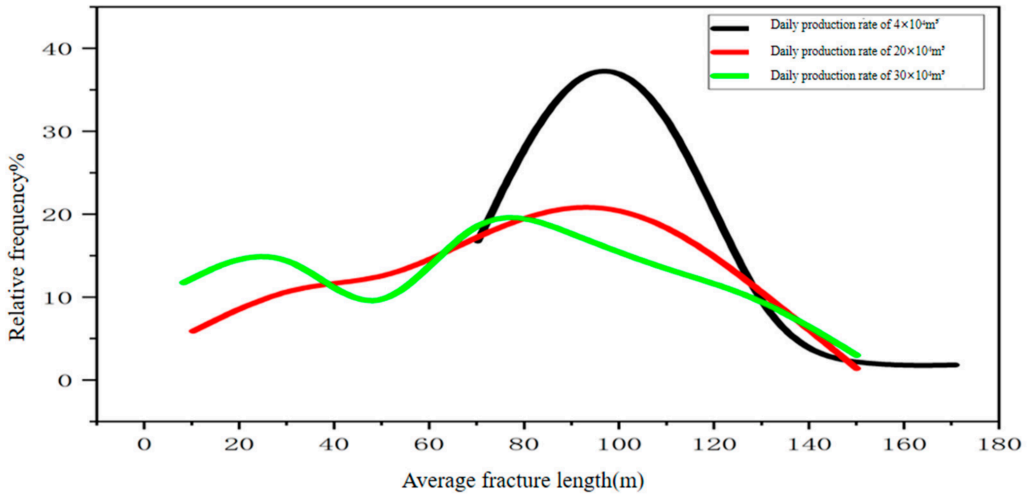


Figure 11. Average fracture length.

The distribution of average fracture height obtained after refracturing following 5 years of production at initial production rates of 4×10^4 m^3/d, 20×10^4 m^3/d, and 30×10^4 m^3/d is shown in Figure 12. The standard deviations of the average fracture height were 17.729, 11.980, and 13.910, respectively. The average fracture heights were 60.204 m, 25.438 m, and 23.522 m, respectively. The results indicate that increasing daily gas production suppresses fracture height growth, and the distribution of fracture height first becomes more concentrated and then more dispersed.

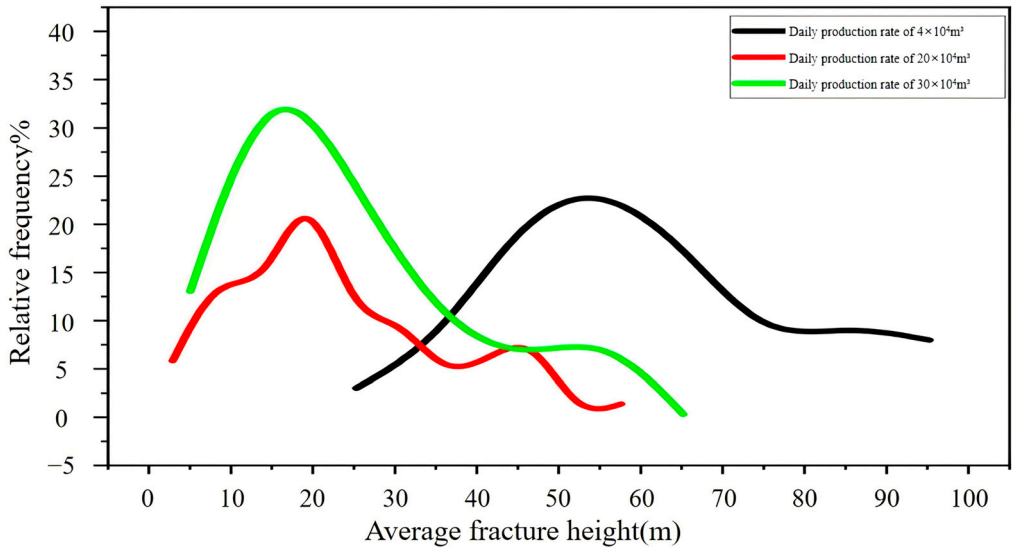


Figure 12. Average fracture height.

The distribution of average fracture width obtained after refracturing following 5 years of production at initial production rates of 4×10^4 m^3/d, 20×10^4 m^3/d, and 30×10^4 m^3/d is shown in Figure 13. The standard deviations of the average fracture width were 3.808, 0.568, and 0.617, respectively. The average fracture widths were 4.613 mm, 1.077 mm, and 0.918 mm, respectively. The results indicate that increasing production rate suppresses fracture width development, and the distribution of fracture width becomes more concentrated.

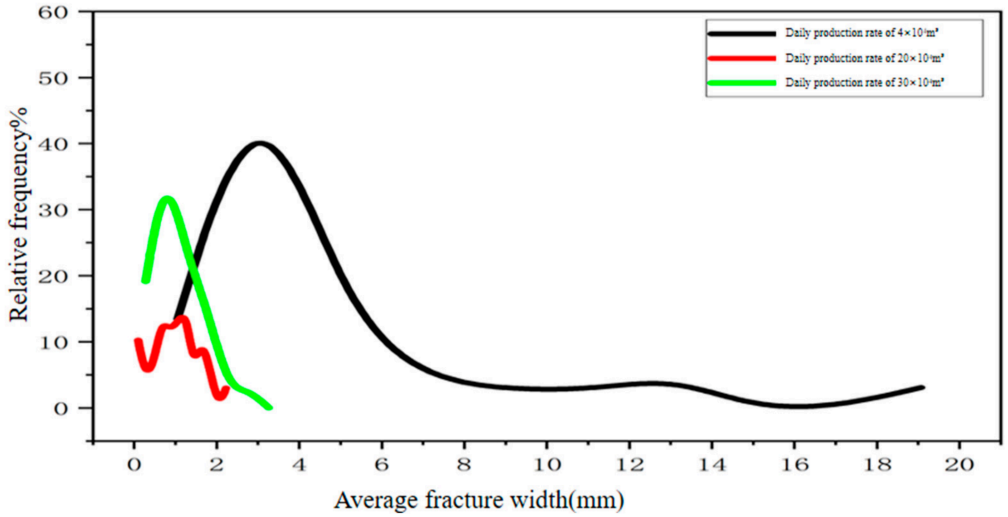
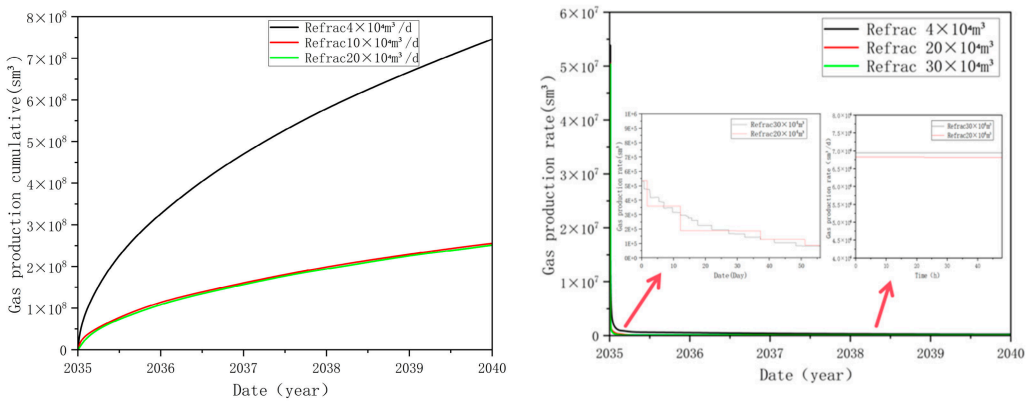


Figure 13. Average fracture width.

3.1.4. Effect of Production Rate on Post-Refracturing Productivity

The cumulative gas production from 2035 to 2040 is shown in Figure 14a, and the gas production rate is presented in Figure 14b. The results indicate that the higher the initial production rate, the lower the production enhancement potential after refracturing. This is because the initial fracturing treatment in high-production wells has already effectively connected natural fractures and formed a complex fracture network, leaving less remaining recoverable reserves available for further stimulation. In contrast, low-production wells, in which the initial fracturing treatment was insufficient, retain more abundant remaining resources, and refracturing can significantly activate previously undeveloped zones. At an initial daily gas production rate of 4×10^4 m^3/d, the cumulative gas production was the highest, while the production increase at 20×10^4 m^3/d was only 0.9% higher than that at 30×10^4 m^3/d.



(**a**) (**b**)

Figure 14. (**a**) Cumulative gas production after refracturing following 5 years of production at production rates of 4×10^4, 20×10^4 and 30×10^4 m^3/d; (**b**) gas production rate after refracturing following 5 years of production at production rates of 20×10^4 m^3/d and 30×10^4 m^3/d.

It should be noted that the cumulative production shown in Figure 14 represents only the simulated post-refracturing production period, rather than the full-life cumulative production including the pre-refracturing production stage. Therefore, the higher post-refracturing cumulative production under the lower initial production-rate case only

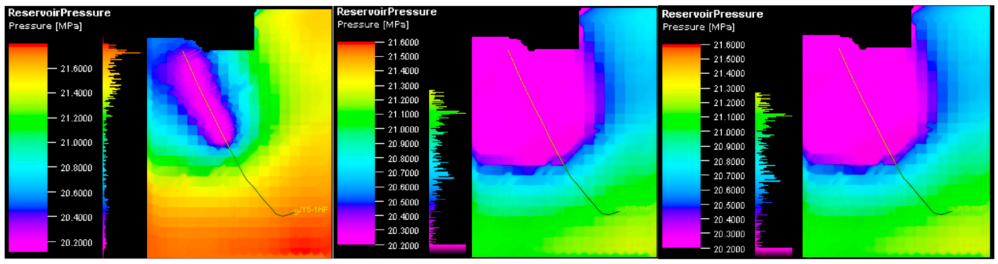
indicates a more favorable response to refracturing, and should not be interpreted as evidence of superior full-life production or economic performance.

3.2. Simulation Results and Interpretation: Initial Production Time

The results of the initial production-rate analysis indicate that 4×10^4 m^3/d is the optimal production rate.

3.2.1. Effect of Initial Production Time on Reservoir Pressure

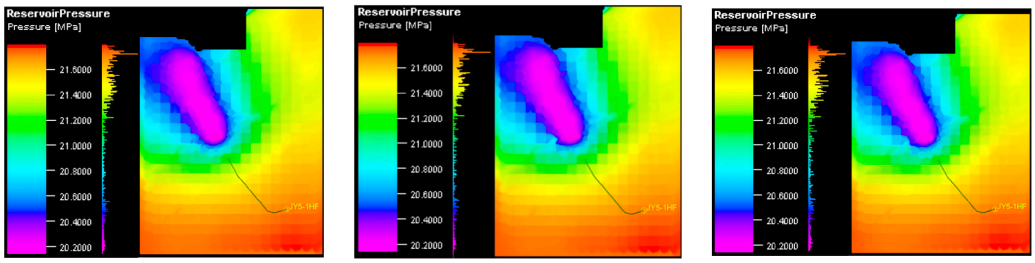
At an initial production rate of 4×10^4 m^3/d, the reservoir pressures obtained after 5, 10, and 20 years of production are shown in Figure 15. The reservoir pressures at a distance of 4 m from the wellbore were 20.14 MPa, 19.26 MPa, and 17.71 MPa, respectively. When the production period was extended to 10 years, the zone of reservoir pressure decline was observed to expand outward from the wellbore. When the production period was further extended to 20 years, the magnitude of reservoir pressure depletion became even more pronounced. It can therefore be concluded that reservoir pressure depletion intensifies with increasing primary production time.



(**a**) (**b**) (**c**)

Figure 15. Reservoir pressure distribution after (**a**) 5 years of production, (**b**) 10 years of production, and (**c**) 20 years of production.

At an initial production rate of 4×10^4 m^3/d, the reservoir pressures obtained after refracturing following 5, 10, and 20 years of production are shown in Figure 16. The reservoir pressures at a distance of 4 m from the wellbore were 20.15 MPa, 20.16 MPa, and 20.17 MPa, respectively. When the production time was extended to 10 years, the reservoir pressure depletion zone was observed to expand outward from the wellbore; however, the extent of this expansion was not significant. When the production period was further extended to 20 years, the extent of reservoir pressure depletion remained essentially unchanged. It can therefore be concluded that, with increasing primary production time, the reservoir pressure at the fracture mouth near the wellbore after refracturing becomes significantly higher than that before refracturing. This study suggests that refracturing reconnected previously unstimulated zones and established communication with new high-pressure "sweet spots."



(**a**) (**b**) (**c**)

Figure 16. Reservoir pressure distribution after refracturing following (**a**) 5 years of production, (**b**) 10 years of production, and (**c**) 20 years of production.

3.2.2. Effect of Initial Production Time on in Situ Stress

To investigate the effect of different primary production times on in situ stress evolution, this study recorded the changes in formation stress at a production rate of 4×10^4 m^3/d after 5, 10, and 20 years of production. The resulting distributions of minimum horizontal principal stress are shown in Figure 17. The minimum horizontal principal stresses at a distance of 4 m from the wellbore were 50.65 MPa, 50.52 MPa, and 50.41 MPa, respectively. When the production period was extended to 10 years, the overall minimum horizontal principal stress of the formation was observed to decline. The localized high-stress zones near the wellbore decreased rapidly during production, and the stress reduction was more pronounced at the fracture roots. Areas with a high degree of depletion were concentrated around the fracture perforation intervals. When the production period was further extended to 20 years, it was observed that the extent of stress reduction near the wellbore became narrower compared to the stress distribution obtained after 5 years of production. The stress reduction at the fracture roots became more pronounced. The area with a high degree of depletion remained concentrated around the fracture perforation intervals. The results indicate that, as production time increases, the overall in situ stress declines. However, once the reservoir enters a deeply depleted stage, pressure depletion can no longer effectively propagate toward the far-field region, causing the depleted zone near the wellbore to shrink instead.

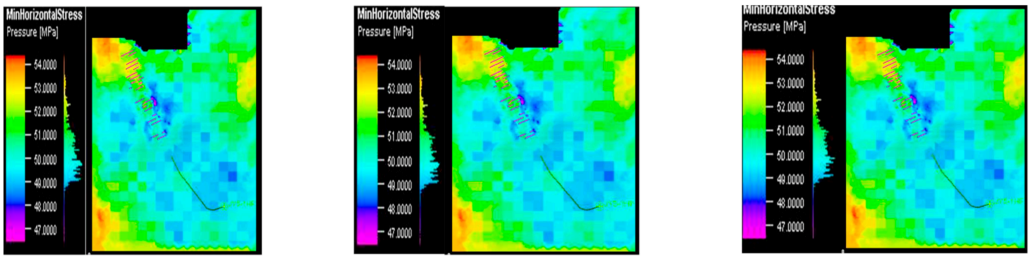


Figure 17. Distribution of minimum horizontal principal stress after initial fracturing at (**a**) 5 years of production, (**b**) 10 years of production, and (**c**) 20 years of production.

Well JY5-1HF was produced at a rate of 4×10^4 m^3/d for 5, 10, and 20 years, respectively, followed by refracturing. The resulting distributions of minimum horizontal principal stress are shown in Figure 18. The minimum horizontal principal stresses at a distance of 4 m from the wellbore were 50.74 MPa, 51.75 MPa, and 47.41 MPa, respectively. When the production period was extended to 10 years, it was observed after refracturing that the reduction in minimum horizontal principal stress near the wellbore was less pronounced than that before refracturing. When the production period was further extended to 20 years, the overall minimum horizontal principal stress of the formation was observed to decrease, with a pronounced stress reduction at the fracture roots. The zones with a high degree of depletion remained concentrated around the fracture perforation intervals. The results indicate that, with increasing production time, the evolution of in situ stress exhibits a trend of initial stabilization followed by gradual depletion.

3.2.3. Effect of Initial Production Time on Fracture Geometry

To investigate the effect of different primary production durations on fracture geometry after refracturing, this study recorded the changes in fracture geometry following refracturing after 5, 10, and 20 years of primary production at a production rate of 4×10^4 m^3/d. When refracturing was performed after 5 years of production, the resulting fracture geometry is shown in Figure 19a. Fracture branching can be observed, generating

new propagation directions that enable the fractures to connect previously unstimulated zones, thereby maximizing the production enhancement potential. When the production period was extended to 10 years, the fracture geometry after refracturing is shown in Figure 19b. Fracture branching, deflection, and extension can be clearly observed. When the production period was further extended to 20 years, the fracture geometry after refracturing is shown in Figure 19c. It can be observed that fracture propagation becomes more difficult, which may potentially induce proppant embedment. This study suggests that prolonged production leads to excessive reservoir pressure depletion, which increases the effective stress in the rock and consequently reduces rock brittleness.

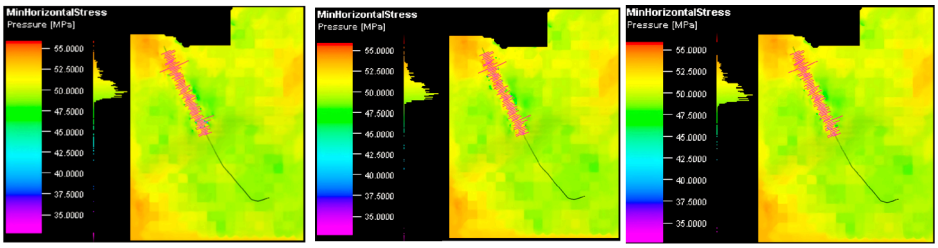


Figure 18. Distribution of minimum horizontal principal stress after refracturing following (**a**) 5 years of production, (**b**) 10 years of production, and (**c**) 20 years of production.

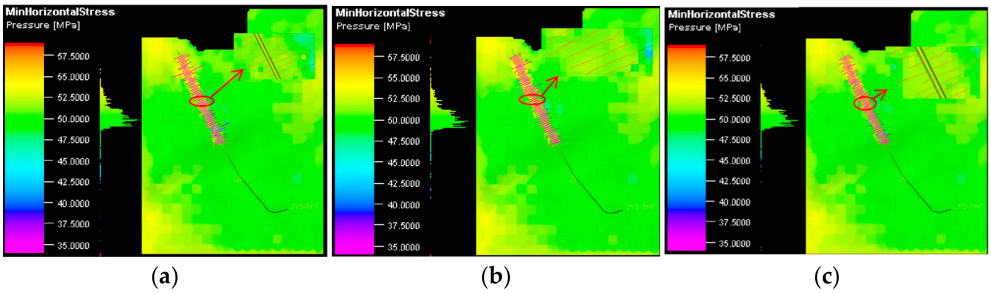


Figure 19. Fracture geometry distribution after refracturing following (**a**) 5 years, (**b**) 10 years, and (**c**) 20 years of primary production.

The variation in average fracture length is shown in Figure 20. At a daily production rate of 4×10^4 m^3/d, the standard deviations of fracture length after 5, 10, and 20 years of production were 27.352, 19.033, and 14.480, respectively, while the corresponding average fracture lengths were 100.61 m, 98.476 m, and 92.818 m. When the production period was extended to 10 years, the fracture length distribution became more concentrated than that obtained after 5 years of production. When the production period was further extended to 20 years, the fracture length distribution became even more concentrated. The results indicate that, with increasing primary production time, the average fracture length exhibits a decreasing trend and its distribution becomes more concentrated.

The variation in average fracture height is shown in Figure 21. At a daily production rate of 4×10^4 m^3/d, the standard deviations of average fracture height after 5, 10, and 20 years of production were 19.374, 17.729, and 18.651, respectively, while the corresponding average fracture heights were 60.806 m, 60.203 m, and 60.738 m. The fracture height distribution obtained after refracturing following 10 years of production was more concentrated than that after 5 years of production, whereas after 20 years of production, the fracture height became more dispersed. The results indicate that, with increasing primary production time, the average fracture height exhibits a trend of first decreasing and then increasing, while its distribution becomes initially more concentrated and subsequently more dispersed.

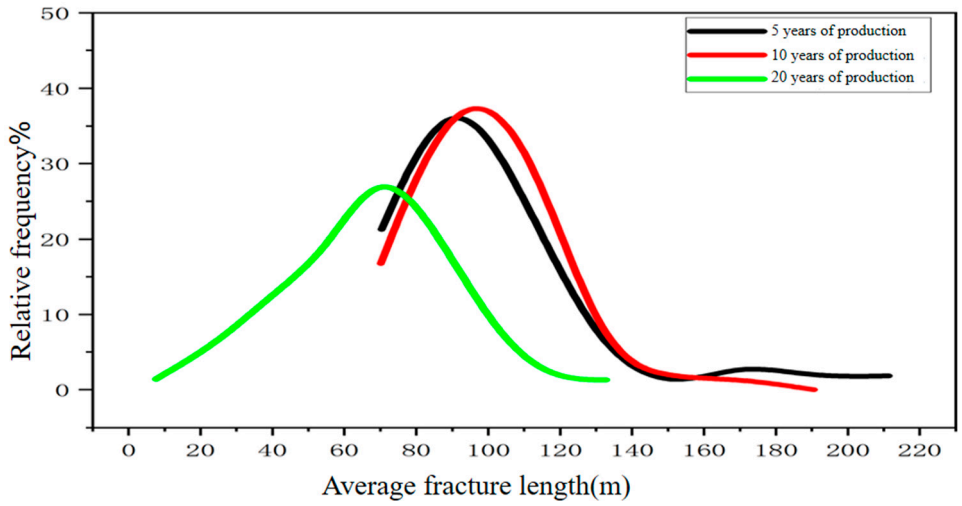


Figure 20. Average fracture length.

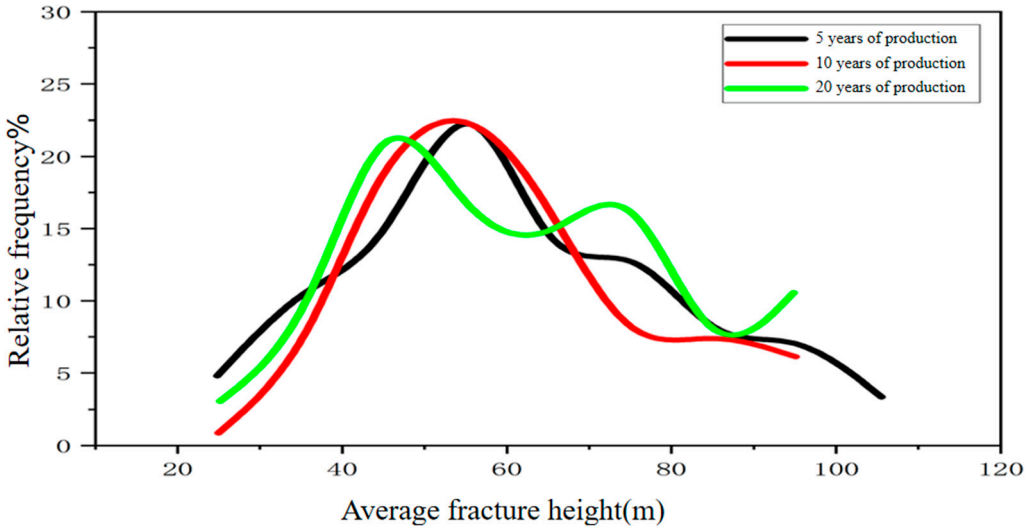


Figure 21. Average fracture height.

The variation in average fracture width is shown in Figure 22. At a daily production rate of 4×10^4 m^3/d, the standard deviations of fracture width after 5, 10, and 20 years of production were 2.998, 3.810, and 3.167, respectively, while the corresponding average fracture widths were 4.970 mm, 4.613 mm, and 4.802 mm. The fracture width distribution obtained after 10 years of production was more dispersed than that obtained after 5 years of production.

When refracturing was performed after extending the production period to 20 years, the fracture width distribution became more concentrated than that obtained after 10 years of primary production. The results indicate that, with increasing primary production time, the average fracture width exhibits a trend of first decreasing and then increasing, while its distribution becomes initially more dispersed and subsequently more concentrated. In summary, this study considers that the mean fracture width remains essentially unchanged, the standard deviations are relatively small, and no clear pattern is observed in the extreme values; therefore, no further analysis of fracture-width variation is presented.

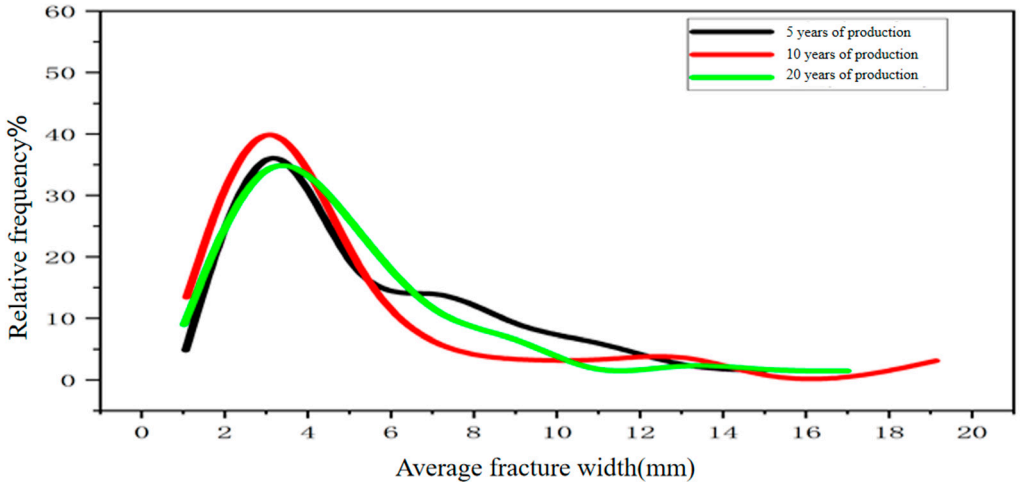


Figure 22. Average fracture width.

3.2.4. Effect of Initial Production Time on Production Performance

As shown in Figure 23a, refracturing after 5 years of primary production yields the highest gas production rate, followed by refracturing after 10 years and 20 years of primary production. The cumulative gas production under different initial production time is shown in Figure 23b, and the highest cumulative production is obtained when refracturing is performed after 5 years of primary production. This study suggests that excessively delayed refracturing results in insufficient formation energy, low fracturing-fluid efficiency, difficulty in fracture propagation, and poor proppant transport and placement performance. Pressure depletion in the near-wellbore region means that even if new fractures are generated, the resulting production enhancement may be limited and short-lived. Reservoir fluid saturation may also undergo unfavorable changes, leading to higher economic risk. In this case study, refracturing after 5 years of primary production was found to be the optimal strategy, yielding a 13.8% increase in production compared with refracturing after 10 years of primary production and a 24.4% increase compared with refracturing after 20 years of primary production.

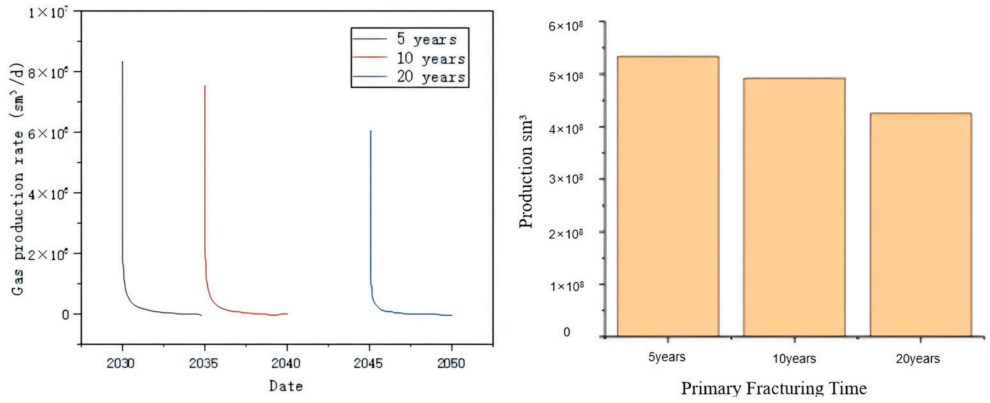


Figure 23. (**a**) Gas production rate and (**b**) cumulative gas production under different initial production time.

3.3. Simulation Results and Interpretation: Water Injection Rate

To clarify the effect of water injection for energy replenishment on reservoir pressure after refracturing, this study selected Well JY5-1HF and conducted refracturing after one year of continuous water injection at rates of 0, 500, 700, and 1000 m^3/d, respectively.

3.3.1. Effect of Water Injection Rate on Reservoir Pressure

The resulting reservoir pressures at a distance of 4 m from the wellbore were 24.58 MPa, 26.07 MPa, 33.74 MPa, and 33.82 MPa, respectively. The reservoir pressure distribution is shown in Figure 24. The simulation results show that water injection for energyreplenishment can effectively increase the reservoir pressure near the wellbore and promote the diffusion of pressure from the wellbore to the surrounding reservoir. Under the condition without water injection, the pressure continues to decline, and the depletion zone expands outward. After moderate water injection (approximately 700 m^3/d), reservoir pressure is significantly restored, and the zone of pressure increase expands markedly, indicating that formation energy is effectively replenished. However, when the water injection rate was further increased to 1000 m^3/d, the extent of the pressure buildup zone showed little further expansion, and the increase in wellbore pressure remained limited, indicating that there exists an effective upper limit for water-injection-based energy replenishment. The results indicate that an appropriate amount of water injection can significantly improve reservoir pressure conditions, whereas excessively high injection rates provide only limited additional benefit for pressure restoration.

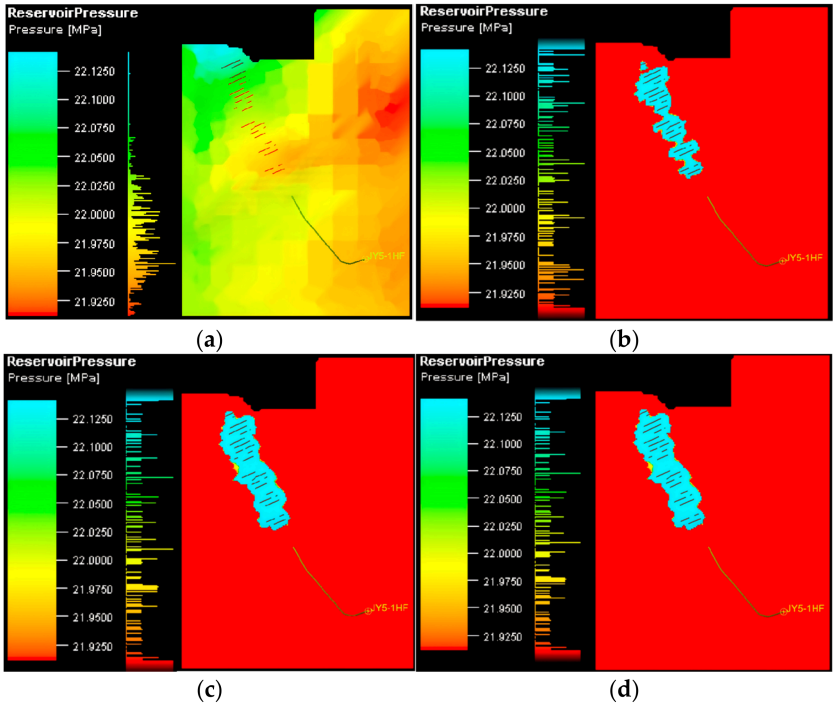


Figure 24. Reservoir pressure under (**a**) no water injection and water injection rates of (**b**) 500 m^3/d, (**c**) 700 m^3/d, and (**d**) 1000 m^3/d.

3.3.2. Effect of Water Injection Rate on in Situ Stress

The resulting minimum horizontal principal stresses at a distance of 4 m from the wellbore were 51.09 MPa, 50.52 MPa, 48.64 MPa, and 48.47 MPa, respectively. The distribution of minimum horizontal principal stress is shown in Figure 25, indicating that water injection for energy replenishment exerts a significant regulatory effect on the minimum horizontal principal stress of the reservoir. Without water injection, the stress near the fracture mouth in the wellbore vicinity remains relatively high, and stress depletion is concentrated mainly at the fracture tips. After moderate water injection (approximately 500–700 m^3/d), the stress-reduction zone extends toward the fracture front and exhibits an elliptical distribution, indicating a marked expansion of the stress-release region. Meanwhile, the stress near the fracture mouth in the wellbore vicinity decreases, suggesting

that formation energy has been redistributed and replenished. However, when the water injection rate was further increased to 1000 m^3/d, the stress distribution remained generally similar to that at 700 m^3/d, and the local stress-regulation effect was not significantly enhanced, indicating that water-injection-based energy replenishment has an effective upper limit. The results indicate that an appropriate amount of water injection can effectively expand the stress-release zone and regulate the in situ stress field, whereas excessively high injection rates provide limited additional improvement in stress control.

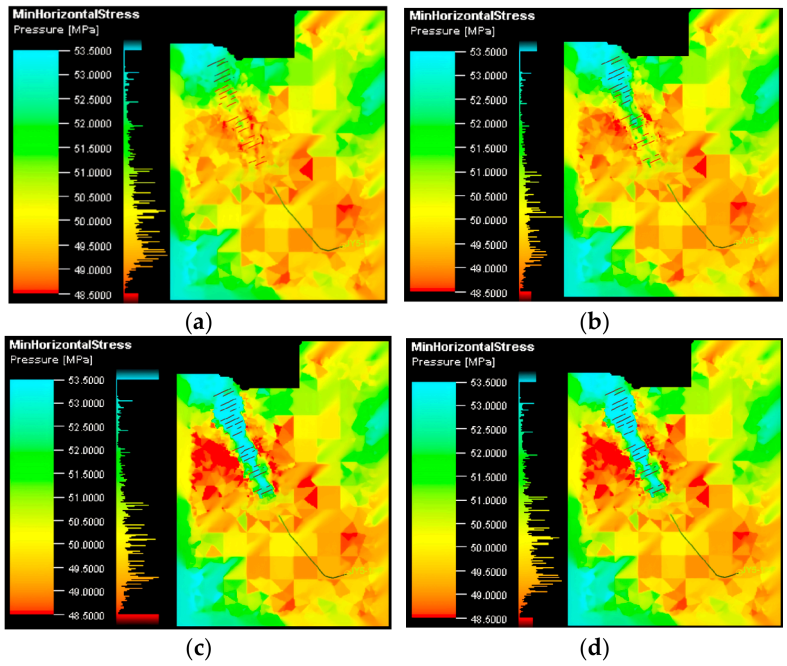


Figure 25. Distribution of minimum horizontal principal stress under (**a**) no water injection and water injection rates of (**b**) 500 m^3/d, (**c**) 700 m^3/d, and (**d**) 1000 m^3/d.

3.3.3. Effect of Water Injection Rate on Refracturing Fracture Geometry

The fracture geometries after refracturing following one year of water injection are shown in Figure 26. It can be clearly observed that the fractures exhibit deflection, extension, and branching, respectively. Based on the above analysis, this study suggests that water injection for energy replenishment reduces the difficulty of fracture initiation and propagation and activates natural fractures as well as weak-plane fractures. As a result, fractures are more likely to undergo deflection, extension, and branching, with increased extension length, thereby substantially promoting the formation of a complex fracture network.

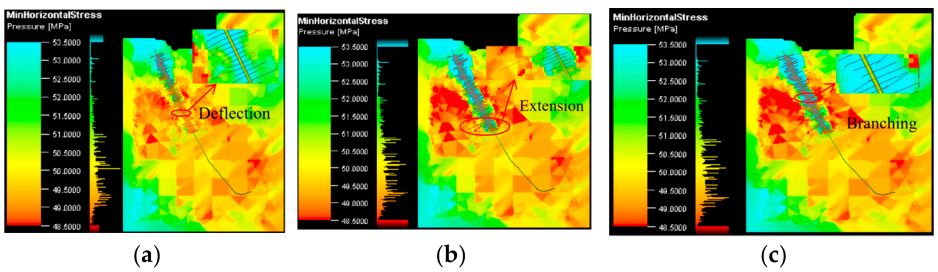


Figure 26. Fracture development after refracturing following 10 years of production at water injection rates of (**a**) 500 m^3/d, (**b**) 700 m^3/d, and (**c**) 1000 m^3/d.

The variation in average fracture length is shown in Figure 27. At water injection rates of 500, 700, and 1000 m^3/d, respectively, the fracture length distributions obtained after one year of water injection were highly dispersed, with standard deviations of 129.72,

39.32, and 28.39, respectively. The average fracture lengths were 134.34 m, 119.26 m, and 114.16 m, respectively. The results indicate that, with increasing water injection rate, the average fracture length first increases and then decreases, while its distribution becomes more concentrated.

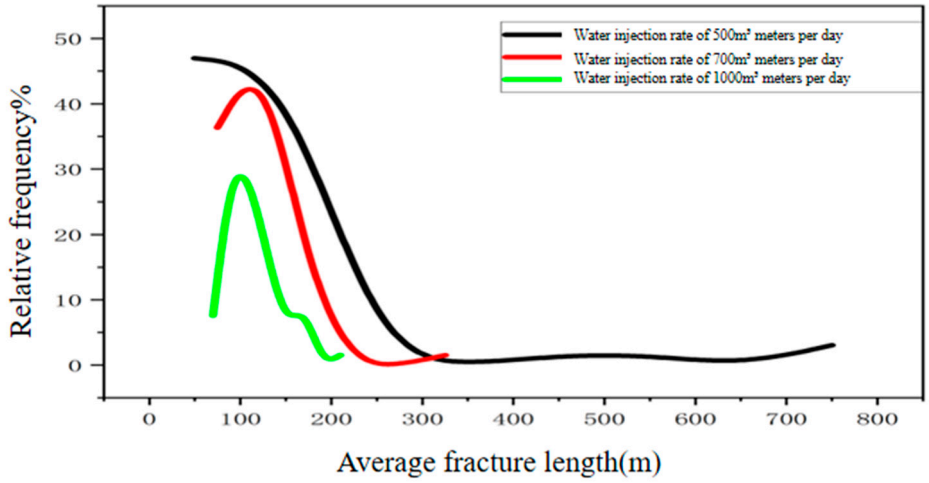


Figure 27. Average fracture length.

The variation in average fracture height is shown in Figure 28. At water injection rates of 500, 700, and 1000 m^3/d, respectively, the standard deviations of the average fracture height after one year of water injection were 18.86, 22.59, and 21.54, respectively. The average fracture heights were 57.93 m, 57.87 m, and 57.14 m, respectively. The results indicate that, with increasing water injection rate, the fracture height distribution first becomes more dispersed and then more concentrated, while the average fracture height changes only slightly.

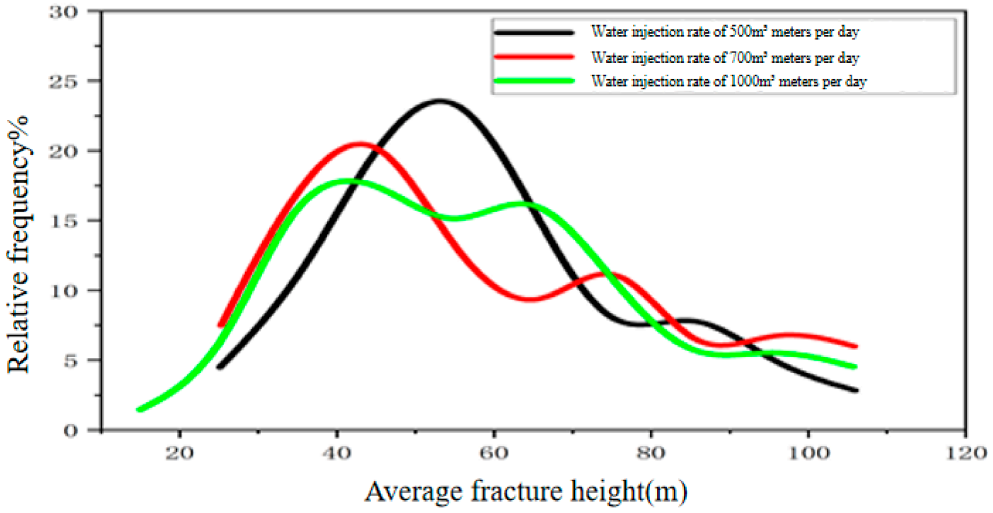


Figure 28. Average fracture height.

The variation in average fracture width is shown in Figure 29. At water injection rates of 500, 700, and 1000 m^3/d, respectively, the standard deviations of the average fracture width after one year of water injection were 3.63, 5.10, and 4.67, respectively, while the corresponding average fracture widths were 4.94 mm, 5.43 mm, and 5.28 mm. The results indicate that the average fracture width first increases and then decreases with increasing water injection rate, while the fracture width distribution exhibits a trend of first becoming more dispersed and then more concentrated.

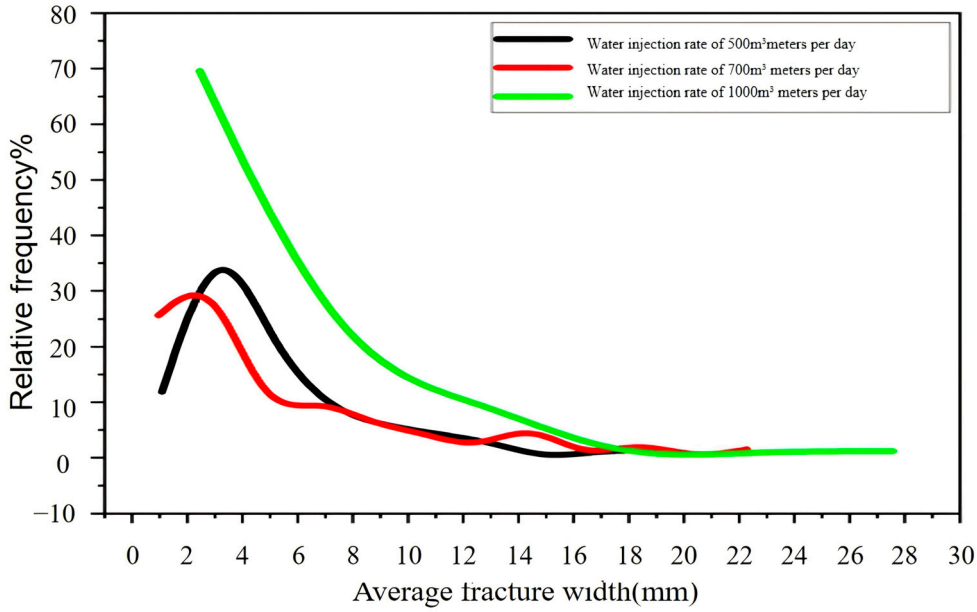
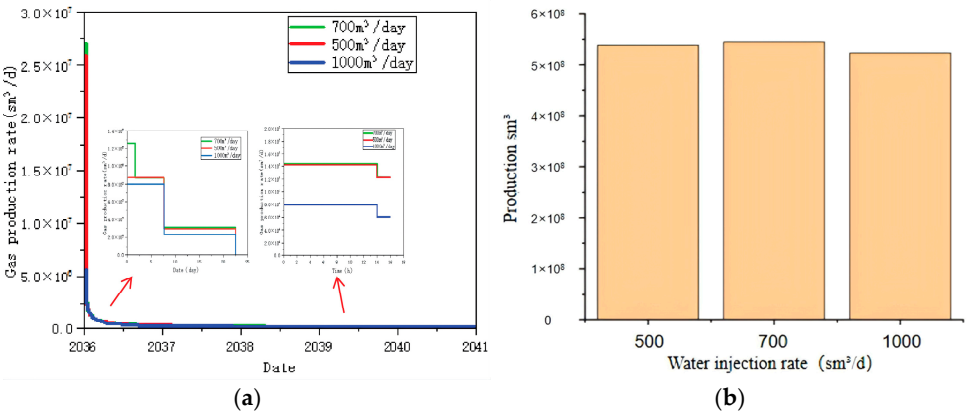


Figure 29. Average fracture width.

3.3.4. Effect of Water Injection Rate on Post-Refracturing Productivity

To investigate the effect of different pre-refracturing water injection rates on production performance, this study analyzed Well JY5-1HF under water injection rates of 500, 700, and 1000 m^3/d. The corresponding production results are shown in Figure 30. As shown in Figure 30a, when refracturing was performed after one year of water injection, the highest gas production rate was obtained at a water injection rate of 700 m^3/d. As shown in Figure 30b, the cumulative gas production was also highest at a water injection rate of 700 m^3/d. Compared with daily water injection rates of 500 m^3/d and 1000 m^3/d, a rate of 700 m^3/d increased production by 1.1% and 4.1%, respectively. It can be concluded that the closer the injection-to-production ratio is to 1, the better the fracture system pressure is maintained, resulting in slower production decline.



(**a**) (**b**)

Figure 30. (**a**) Gas production rate and (**b**) cumulative gas production under different water injection rates.

It should be noted that the parameter selection in this study was mainly based on the post-refracturing production response and changes in the pressure–stress fields. A full-life cumulative production comparison including the pre-refracturing production stage and an economic evaluation were not conducted. Therefore, the selected parameter combination represents only a technically favorable strategy under the simulated conditions of this

study and should not be regarded as a global optimum in terms of full-life production or economic performance.

4. Conclusions

This study quantitatively evaluated the effects of initial production rate, primary production time, and water-injection energy-replenishment rate on reservoir pressure depletion, in situ stress evolution, and refracturing-induced fracture development in the target block of the Fuling shale gas field. The conclusions are mainly applicable to the Fuling Block, and the main findings are as follows:

1. The initial production rate directly controls the degree of reservoir pressure depletion and in situ stress redistribution. When the production rate increased from 4×10^4 m^3/d to 30×10^4 m^3/d, the wellbore pressure decreased from 22.02 MPa to 4.33 MPa, while the minimum horizontal principal stress at the fracture root declined from 49.47 MPa to 47.60 MPa, resulting in a significant expansion of the near-wellbore stress-perturbation zone. The development of refracturing-induced fractures is increasingly suppressed as the production rate rises, with fracture length decreasing by 19.94–27.29% (calculated as the ratio of the average reduction in length to the original length) and fracture width by 76.74–80.00%, indicating that both fracture propagation capacity and fracture-network complexity are significantly weakened. At the same time, the production enhancement effect of refracturing is more limited for high initial production wells. The production increase under a production rate of 20×10^4 m^3/d is only 0.9% higher than that under 30×10^4 m^3/d conditions.
2. The primary production time governs reservoir energy depletion and stress field evolution. When the production time was extended from 5 years to 20 years, the wellbore pressure decreased from 20.14 MPa to 17.71 MPa. Although in situ stress continued to decline, the extent of stress adjustment significantly narrowed, indicating that after long-term depletion, the space for stress regulation is limited. Fracture propagation capacity gradually decreases with increasing production time, with fracture length declining from 100.61 m to 92.82 m. Fracture branching and network complexity are also significantly weakened, thereby limiting the effectiveness of refracturing. Under the simulated conditions, refracturing after approximately 5 years of primary production showed a more favorable post-refracturing production response, with cumulative post-refracturing production being 13.8% and 24.4% higher than those under the 10-year and 20-year cases, respectively.
3. Water injection for energy replenishment can effectively increase reservoir pressure and regulate the in situ stress distribution. The wellbore pressure increased from 24.58 MPa under the no-injection condition to 33.74 MPa at an injection rate of 700 m^3/d, whereas the increment tended to stabilize at 1000 m^3/d, indicating that the effectiveness of water-injection-based energy replenishment has an upper limit. The extent of in situ stress adjustment is more favorable at an injection rate of 700 m^3/d, beyond this rate, the stress-recovery zone shows little further expansion. Fracture geometry also varies with water injection rate: at 500 m^3/d, fractures are more likely to undergo deflection; at 700 m^3/d, fracture extension capacity is the strongest; whereas at 1000 m^3/d, fractures are more prone to branching. Fracture length increased by 20.10% at 700 m^3/d compared to 500 m^3/d, but then decreased by 4.2% at 1000 m^3/d. Production performance indicates that 700 m^3/d provides a more favorable water-injection rate for energy replenishment under the simulated conditions, with post-refracturing production being 1.1% and 4.1% higher than that at 500 m^3/d and 1000 m^3/d, respectively.

This study has several limitations. The proposed parameter combination is mainly supported by the post-refracturing production and stress responses, without considering full-life cumulative production including the pre-refracturing production stage or economic indicators such as net present value, investment cost, and operating cost. Therefore, this parameter combination should be interpreted as a technically favorable strategy under the simulated conditions of this study rather than a global optimum. Future studies should integrate full-life production forecasting and economic evaluation to further assess its overall applicability.

Author Contributions: Conceptualization, P.L. and Y.L.; methodology, P.L.; software, Y.M., Y.G., C.X. and J.D.; validation, Y.M., Y.G., C.X. and J.D.; formal analysis, Y.L.; investigation, P.L.; resources, S.T.; data curation, Y.L.; writing—original draft preparation, Y.L.; writing—review and editing, P.L., Y.L. and S.T.; visualization, Y.M., Y.G., C.X. and J.D.; supervision, S.T.; project administration, S.T.; funding acquisition, S.T. All authors have read and agreed to the published version of the manuscript.

Funding: This study was founded by National Science and Technology Major Project of China (Grant No. 2025ZD1404104). Xinjiang Key Laboratory of Carbon Efficient Utilization and Storage (Grant No. XJCCUS202508); the Autonomous Region Key Research and Development Project (Grant No. 2024B01013), and Xinjiang Uygur Region "One Case, One Policy" Strategic Talent Introduction Project (Grant No. XQZX20240054).

Data Availability Statement: The data presented in this study are available on request from the corresponding author. (The data are not publicly available due to privacy or ethical restrictions.)

Acknowledgments: The authors gratefully acknowledge the technical support received during the preparation of this manuscript. We declare that OpenAI ChatGPT (4.0) was used solely for language polishing, grammar correction, and optimization of academic English expression in the final manuscript. The AI tool was not involved in any stage of the research process, including but not limited to research design, data collection and processing, experimental result analysis, core argument development, figure or chart preparation, and scientific interpretation. All AI-assisted language content has been carefully reviewed, revised, and confirmed by all authors. The authors take full responsibility for the originality, accuracy, and integrity of the manuscript, as well as all final decisions related to its submission and publication.

Conflicts of Interest: Author Peng Li was employed by the company Sinopec Chongqing Fuling Shale Gas Exploration and Development Co., Ltd. The remaining authors declare that the research was conducted in the absence of any commercial or financial relationships that could be construed as a potential conflict of interest.

References

1. Chen, Y.; Zhang, Y. Shale Gas Transition in China: Evidence Based on System Dynamics Model for Production Prediction. *Energies* **2025**, *18*, 878. [CrossRef]
2. Gao, M.; Liu, H.; Wang, Y.; Hu, X.; Liu, C.; Yu, W. Investigation into the Quantitative Assessment of Reserve Mobilization in Horizontal Well Groups Within the Southern Sichuan Shale Gas Reservoir. *Energies* **2025**, *18*, 4910. [CrossRef]
3. Li, G.; Wang, G.; Xiong, W.; Feng, N.; Chen, F.; Bi, R.; Pan, Y.; Zheng, J.; Feng, Y.; Lu, C.; et al. Lower Cambrian Shale Gas in Southern China: A Review of Distribution, Geochemical Characteristics, and Its Genesis Mechanism. *ACS Omega* **2025**, *10*, 51848–51868. [CrossRef] [PubMed]
4. Liu, S.; Ma, W.; Jansa, L.; Huang, W.; Zeng, X.; Zhang, C. Characteristics of the shale gas reservoir rocks in the Lower Silurian Longmaxi Formation, East Sichuan basin, China. *Energy Explor. Exploit.* **2013**, *31*, 187–219. [CrossRef]
5. Han, C.; Liu, G.; Ma, C.; Qi, M.; Yang, Y.; Li, G. Influencing Factors of Shale Permeability in the Longmaxi Formation, Southern Sichuan Basin and Northern Yunnan-Guizhou Depression. *Geofluids* **2022**, *2022*, 6832272. [CrossRef]
6. Chuanxiang, S.; Haikuan, N.; Haikun, S.; Wei, D.; Ting, L.; Yalin, C.; Mi, L.; Jingchang, L. Porosity, permeability and rock mechanics of Lower Silurian Longmaxi Formation deep shale under temperature-pressure coupling in the Sichuan Basin, SW China. *Pet. Explor. Dev.* **2023**, *50*, 85–98. [CrossRef]
7. Xusheng, G.; Ruyue, W.; Baojian, S.; Guanping, W.; Chengxiang, W.; Qianru, W. Geological characteristics, resource potential, and development direction of shale gas in China. *Pet. Explor. Dev.* **2025**, *52*, 17–32. [CrossRef]

8. Rutqvist, J.; Rinaldi, A.P.; Cappa, F.; Moridis, G.J. Modeling of fault reactivation and induced seismicity during hydraulic fracturing of shale-gas reservoirs. *J. Pet. Sci. Eng.* **2013**, *107*, 31–44. [CrossRef]
9. Nie, H.; Li, D.; Liu, G.; Lu, Z.; Hu, W.; Wang, R.; Zhang, G. An overview of the geology and production of the Fuling shale gas field, Sichuan Basin, China. *Energy Geosci.* **2020**, *1*, 147–164. [CrossRef]
10. Wang, X.-H.; Zhang, F.-S.; Yin, Z.-R.; Weng, D.-W.; Liang, H.-B.; Zhou, J.-P.; Xu, B. Numerical investigation of refracturing with/without temporarily plugging diverters in tight reservoirs. *Pet. Sci.* **2022**, *19*, 2210–2226. [CrossRef]
11. Xu, L.; Wang, D.; Liu, L.; Wang, C.; Zhu, H.; Tang, X. Review of shale oil and gas refracturing: Techniques and field applications. *Processes* **2024**, *12*, 965. [CrossRef]
12. Liang, H.; Bao, P.; Hui, G.; Ma, Z.; Yan, X.; Bai, X.; Ren, J.; Pi, Z.; Li, Y.; Ge, C. Simulation Study of Refracturing of Shale Oil Horizontal Wells Under the Effect of Multi-Field Reconfiguration. *Processes* **2025**, *13*, 1915. [CrossRef]
13. Shah, M.; Shah, S.; Sircar, A. A comprehensive overview on recent developments in refracturing technique for shale gas reservoirs. *J. Nat. Gas Sci. Eng.* **2017**, *46*, 350–364. [CrossRef]
14. Tao, X.; Gan, M.; Yao, Z.; Bai, J.; Yang, M.; Su, G.; Zheng, L. Enhancing the production of tight sandstone gas well through fuzzy-ball fluid temporary plugging with diverting fractures and water cutting after refracturing in one operation. *J. Pet. Sci. Eng.* **2022**, *217*, 110883. [CrossRef]
15. Zhang, X.; Ren, J.; Feng, Q.; Wang, X.; Wang, W. Prediction of refracturing timing of horizontal wells in tight oil reservoirs based on an integrated learning algorithm. *Energies* **2021**, *14*, 6524. [CrossRef]
16. Shi, D.; Cheng, S.; Bai, W.; Liu, X.; Cai, D. Numerical Simulation of Fracture Propagation Induced by Water Injection in Tight Oil Reservoirs. *Processes* **2024**, *12*, 1767. [CrossRef]
17. Zhengdong, L.; Zhengmao, W.; Lijun, M.; Huanhuan, P.; Xin, L.; Xiaohu, B.; Zhen, T.; Hongchang, L.; Yingfeng, P. A technique for enhancing tight oil recovery by multi-field reconstruction and combined displacement and imbibition. *Pet. Explor. Dev.* **2024**, *51*, 152–163. [CrossRef]
18. Ding, C.; Guo, X.; Xiao, C.; Sui, Z.; Yang, Y. Experimental Study on the Influence of Blast Hole Bottom Cushion Medium on Blasting Damage Characteristics and Strain Evolution of Rock Mass. *Rock Mech. Rock Eng.* **2025**, *58*, 1895–1909.
19. Zhang, L.; Kan, Z.; Zhang, C.; Tian, S.; Zeng, S.; Hao, D. Permeability and stress sensitivity of coals with different fracture directions under cyclic loading–unloading conditions: A case study of the Xutuan Coal Mine in Huaibei Coalfield, China. *Rock Mech. Rock Eng.* **2026**, *59*, 951–969.
20. Yang, J.; Fan, P.; Wang, M.; Li, J.; Qian, Q. Perturbation-induced delayed shear creep instability in rock Joints: A nonlinear model based on irreversible deformation. *Int. J. Rock Mech. Min. Sci.* **2025**, *195*, 106289. [CrossRef]
21. Li, X.; Wang, J.; Elsworth, D. Stress redistribution and fracture propagation during restimulation of gas shale reservoirs. *J. Pet. Sci. Eng.* **2017**, *154*, 150–160. [CrossRef]
22. Dong, Q.; Li, J.; Yang, L.; Wang, F.; Zhao, K.; Huo, F. Research on Refracturing Technology of Horizontal Wells Based on Dynamic Drainage Volume. *Front. Energy Res.* **2022**, *10*, 864527. [CrossRef]
23. Shi, X.; Ge, X.; Gao, Q.; Han, S.; Zhang, Y.; Kong, X. Numerical simulation of hydraulic fracture propagation from recompletion in refracturing with dynamic stress modeling. *Geomech. Geophys. Geo-Energy Geo-Resour.* **2024**, *10*, 155. [CrossRef]
24. Lake, L.W.; Johns, R.; Rossen, B.; Pope, G.A. *Fundamentals of Enhanced Oil Recovery*; Society of Petroleum Engineers: Richardson, TX, USA, 2014; Volume 1.
25. Zhou, Q.; Dai, R.; Chen, L.; Wu, C.; Luo, S. Optimization of refracturing timing in tight oil reservoirs based on an oil water two phase flow model. *Sci. Rep.* **2025**, *15*, 22907. [CrossRef] [PubMed]
26. Deng, Y.; Mu, S.; Liu, Y.; Mu, N.; Guo, J.; Zeng, J.; Yu, H. Numerical simulation of stress field reorientation in multi-fractures. *Geomech. Geophys. Geo-Energy Geo-Resour.* **2024**, *10*, 36. [CrossRef]
27. Dai, J.; Ma, Z.; Yue, Y.; Yuan, Y.; Tian, S. Thermo-hydro-chemical coupled numerical modeling of hydrogen-thermal co-development in hydraulically fractured peridotite. *Adv. Geo-Energy Res.* **2026**, *20*, 145–162. [CrossRef]
28. Zhou, R.; Yuan, Y.; Dai, J.; Tian, S.; Mu, Z.; Li, G. Study on the adsorption and diffusion behavior of natural hydrogen in olivine and serpentine. *Int. J. Hydrogen Energy* **2026**, *247*, 155919. [CrossRef]
29. Shi, S.; Shi, C.; Tian, G.; Lin, B.; Yu, H.; Wei, S.; Wang, Z. Stress evolution and fracture propagation of infill well after production and injection of parent well in a tight oil reservoir. *J. Pet. Explor. Prod. Technol.* **2023**, *13*, 1135–1153. [CrossRef]
30. Ren, G.; Ma, X.; Zhang, S.; Zou, Y.; Duan, G.; Xiong, Q. Optimization of Water Injection Strategy before Re-Stimulation Considering Fractures Propagation. *Processes* **2022**, *10*, 1538. [CrossRef]
31. Qiang, W.; Jinzhou, Z.; Yongquan, H.; Yongming, L.; Yufeng, W. Optimization method of refracturing timing for old shale gas wells. *Pet. Explor. Dev.* **2024**, *51*, 213–222. [CrossRef]
32. Yin, Z.; Zhang, F.; Wang, X.; Zhang, L.; Zhu, H. Four-dimensional stress induced by hydraulic fracturing and long-term extraction for shale gas well platforms: Implications for refracturing design. *J. Rock Mech. Geotech. Eng.* **2026**, *18*, 4349–4366.
33. Shi, W.; Li, J.; Huang, Z.; Feng, Y.; Hong, P.; Lei, S.; Wu, Y.; Wang, J.; Guo, M. Refracturing shale gas wells in China: Doubling water consumption for enhanced gas recovery. *Sci. Total Environ.* **2024**, *946*, 174407. [CrossRef] [PubMed]

34. Allawi, R.H.; Al-Jawad, M.S. Wellbore instability management using geomechanical modeling and wellbore stability analysis for Zubair shale formation in Southern Iraq. *J. Pet. Explor. Prod. Technol.* **2021**, *11*, 4047–4062. [CrossRef]
35. Lekhnitskii, S.G.; Fern, P.; Brandstatter, J.J.; Dill, E. *Theory of Elasticity of an Anisotropic Elastic Body*; American Institute of Physics: College Park, MD, USA, 1964.
36. Mavko, G.; Mukerji, T.; Dvorkin, J. *The Rock Physics Handbook*; Cambridge University Press: Cambridge, UK, 2020.
37. Ahmed, T. *Reservoir Engineering Handbook*; Gulf Professional Publishing: Oxford, UK, 2018.
38. Zoback, M.D. *Reservoir Geomechanics*; Cambridge University Press: Cambridge, UK, 2010.

Disclaimer/Publisher's Note: The statements, opinions and data contained in all publications are solely those of the individual author(s) and contributor(s) and not of MDPI and/or the editor(s). MDPI and/or the editor(s) disclaim responsibility for any injury to people or property resulting from any ideas, methods, instructions or products referred to in the content.